Environmental Science & Technology

pubs.acs.org/est

Article

Fabrication of Highly Dispersed Ru Catalysts on CeO_2 for Efficient C_3H_6 Oxidation

Bifeng Zhang, Jiawei Yang, Yibo Mu, Xiaoyu Ji, Yandi Cai, Nan Jiang, Shaohua Xie, Qiuhui Qian, Fudong Liu,* Wei Tan,* and Lin Dong

Cite This: *Environ. Sci. Technol.* 2024, 58, 19533−19544

Read Online

ACCESS | Metrics & More | Article Recommendations | Supporting Information

ABSTRACT: Emissions of volatile organic compounds (VOCs) threaten both the environment and human health. To realize the elimination of VOCs, Ru/CeO_2 catalysts have been intensively investigated and applied. Although it has been widely acknowledged that the catalytic performance of platinum group metal catalysts was highly determined by their dispersion and coordination environment, the most reactive structures on Ru/CeO_2 catalysts for VOCs oxidation are still ambiguous. In this work, starting from Ce-BTC (BTC = 1,3,5-benzenetricarboxylic acid) materials, atomically dispersed Ru catalysts and agglomerated Ru catalysts were successfully created via one-step hydrothermal method (Ru-CeO_2-BTC) and conventional incipient wetness impregnation method (Ru/CeO_2-BTC), respectively. In a typical model reaction of C_3H_6 oxidation, atomically dispersed $Ru^{\delta+}$ species with the formation of abundant Ru−O−Ce linkages on Ru-CeO_2-BTC were found to perform much better than agglomerated RuO_x species on Ru/CeO_2-BTC. Further characterizations and mechanism study disclosed that Ru-CeO_2-BTC catalyst with atomically dispersed Ru ions and more superior low temperature redox performance compared to Ru/CeO_2-BTC could better facilitate the adsorption/activation of C_3H_6 and the decomposition/desorption of intermediates, thus exhibiting superior C_3H_6 oxidation activity. This work elucidated the reactive sites on Ru/CeO_2 catalysts in the C_3H_6 oxidation reaction and provided insightful guidance for designing efficient Ru/CeO_2 catalysts to eliminate VOCs.

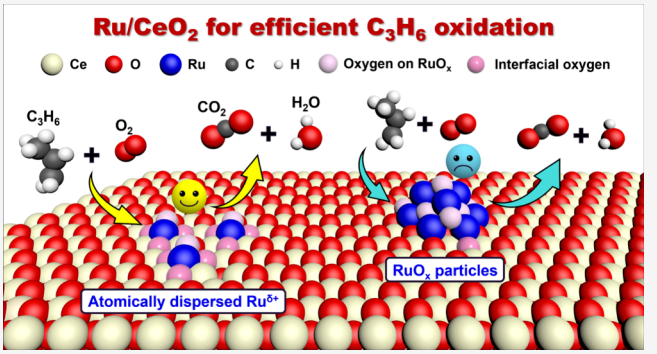

KEYWORDS: *Ce-BTC, one-step hydrothermal method, dispersion of RuO_x, C_3H_6 oxidation, Ru−O−Ce structure*

1. INTRODUCTION

Volatile organic compounds (VOCs) emitted from various sources (e.g., domestic use, industry, motor vehicles, etc.) can pose a significant threat to both the ecological environment and human health. To reduce the emissions of VOCs, many strategies have been developed, and catalytic oxidation has been verified to be one of the most efficient.[1−5] Among those catalysts developed for catalytic oxidation of VOCs, platinum group metals (PGMs), such as Pt, Pd, Ru, etc., supported on stable metal oxides (Al_2O_3, CeO_2, ZrO_2, etc.) exhibited the most satisfactory catalytic performance.[6−12] Considering the cost-effectiveness, Ru catalysts with much lower prices than Pd and Pt catalysts and decent catalytic performance have attracted tremendous research interest. Due to the nature of CeO_2 based materials to form strong interactions with Ru and the resulting efficient electron/oxygen transfer at the Ru-CeO_2 interface, Ru/CeO_2 catalysts exhibiting superior catalytic oxidation performance have been intensively investigated.[13−17]

In recent decades, it has been widely reported that the dispersion or the coordination environment of PGMs showed a significant impact on their catalytic oxidation performance.[18−23] For example, Gänzler et al. systematically analyzed *in situ* time-resolved X-ray absorption spectroscopy (XAS) of Pt/CeO_2-Al_2O_3 catalysts in a dynamic reducing/oxidating cycling test and determined that the optimal size for Pt clusters supported on CeO_2-Al_2O_3 support in CO oxidation reaction was 1.4 nm, since Pt clusters with such size could provide the maximum Pt-CeO_2 interfacial sites and facilitate the activation of CeO_2 to participate in the redox cycle.[19] In addition to the dispersion, the coordination environment of PGMs sites might also play a vital role. Previously, we reported that the CO oxidation activity on Pt/Pd single atoms or clusters on CeO_2 could be boosted by tuning their coordination environment, and such a strategy could be generalized to the preparation of catalysts for the elimination of various air pollutants.[22]

Received: July 13, 2024
Revised: September 17, 2024
Accepted: September 18, 2024
Published: September 26, 2024

However, different from the significant achievement in determining active sites on Pt(Pd)/CeO_2 catalysts, the optimal dispersion and local coordination environments of Ru sites on Ru/CeO_2 catalysts were still ambiguous, especially in the catalytic oxidation of VOCs. Therefore, it is definitely necessary to construct Ru/CeO_2 catalysts with different Ru dispersion or local coordination environments as model catalysts to help understand the structure−activity relationship on Ru/CeO_2 catalysts.

Recently, to realize the facile modulation of Ru dispersion on CeO_2, support engineering strategies, including morphology control,[13,15,16] additives modification,[24,25] and surface defect engineering,[26−32] were developed and widely applied. For example, Li et al. systematically investigated the influence of the morphology of CeO_2 on the dispersion of Ru and Ru−CeO_2 interaction and disclosed that the strong metal−support interaction between Ru and CeO_2-NR could better facilitate the dispersion and stabilization of Ru species.[15] It was also reported that atomically dispersed Ru single atoms on a nanoflower-like CeO_2 support exhibited remarkable stability and soot oxidation activity, and even rivaled commercial Pt catalysts.[33] Besides, Liu et al. disclosed that the surface hydroxyl groups at the step/edge sites on the surface of CeO_2 would also determine the dispersion behavior of Ru species, and the atomically dispersed Ru species anchored at the step sites exhibited superior C_3H_6 oxidation activity.[31] That is, the development of facile methods for the synthesis of Ru/CeO_2 catalysts with tunable Ru dispersion and the identification of real active sites on Ru/CeO_2 catalysts are research hotspots in developing Ru/CeO_2 catalysts with superior catalytic oxidation performance.

Metal−organic frameworks (MOFs) with large surface area and tunable porous structures, such as Ce-BTC (BTC = 1,3,5-benzenetricarboxylic acid), have been recognized as an ideal precursor for synthesizing CeO_2 with high specific surface area and abundant surface defects, which could be used as superior supports for boosting the catalytic performance of supported PGMs or transition metal species.[34−37] Besides, when targeted active metal species were introduced during the preparation of Ce-MOFs instead of being impregnated onto Ce-BTC or CeO_2 derived from Ce-BTC, active metal species could be well mixed with Ce sites, thus generating highly dispersed metal species with strong PGMs−CeO_2 interactions.

Building on the above understandings, herein, atomically dispersed Ru species and agglomerated Ru species were successfully constructed on CeO_2 derived from Ce-BTC through one-step hydrothermal method and conventional incipient impregnation method, respectively. When the prepared Ru catalysts were applied in the catalytic oxidation of C_3H_6, a common VOC emitted by both mobile and stationary sources, it was found that atomically dispersed $Ru^{\delta+}$ species performed much better than agglomerated RuO_x species, under the condition of the same Ru loading. Such difference should be due to that highly dispersed $Ru^{\delta+}$ species supported on CeO_2 with the formation of more Ru−O−Ce linkages exhibited better redox performance and could better facilitate the adsorption/activation of C_3H_6 and the decomposition/desorption of intermediates than agglomerated RuO_x species on CeO_2.

2. MATERIALS AND EXPERIMENTAL METHODS

2.1. Catalyst Preparation. Ru-CeO_2-BTC catalysts with different Ru loadings were prepared by a one-step hydrothermal method.[37] Specifically, cerium nitrate hexahydrate, ruthenium acetylacetonate, and 1,3,5-benzenetricarboxylic acid (BTC, 4.8 mmol) were first dissolved in 40 mL of *N*,*N*-dimethylformamide (DMF) under vigorous stirring at room temperature. After further stirring for 30 min, the mixture was transferred to an autoclave and heated at 130 °C for 20 h. After the autoclave was cooled to room temperature, the resulting mixture was washed with DMF and ethanol several times. Afterward, the obtained gel was dried at 100 °C overnight and subsequently calcined at 450 °C for 3 h with a ramping rate of 5 °C·min^{-1}. The total metal content (Ru + Ce) was controlled at 8 mmol, and the theoretical Ru weight ratios of the prepared catalysts were 0, 1.4, 2.8, and 5.3 wt %. By using inductively coupled plasma atomic emission spectroscopy (ICP-AES), the actual Ru loadings were determined as 0, 1.4, 2.4, and 3.3 wt %. The obtained catalysts were denoted as *x*Ru-CeO_2-BTC, in which *x* in wt % was the actual Ru loadings, and the catalyst without the addition of Ru was denoted as CeO_2-BTC. Meanwhile, the uncalcined samples were denoted as Ce-BTC or *x*Ru-Ce-BTC. The 2.4Ru/CeO_2-BTC catalyst was prepared by a hydrothermal-impregnation two-step method. First, 2.4 wt % Ru (using $Ru(NO)(NO_3)_m(OH)_n$ as a precursor, $m + n = 3$) was loaded on CeO_2-BTC through the conventional incipient wetness impregnation (IWI) method. After being dried at 120 °C for 20 min, the mixture was calcined at 450 °C for 3 h with a ramping rate of 5 °C·min^{-1}.

Ru (2.4 wt %, using $Ru(NO)(NO_3)_m(OH)_n$ as a precursor, $m + n = 3$) loaded on commercial CeO_2 (CeO_2-C), CeO_2 nanorod synthesized by hydrothermal method (CeO_2-NR),[38] CeO_2 nanoparticles obtained by thermal decomposition of $Ce(NO_3)_3{\cdot}6H_2O$ (CeO_2-NP), rutile TiO_2 and Al_2O_3 were prepared by an IWI method and used as reference samples, which were denoted as 2.4Ru/CeO_2-C, 2.4Ru/CeO_2-NR, 2.4Ru/CeO_2-NP, 2.4Ru/TiO_2-Rut and 2.4Ru/Al_2O_3, respectively. Meanwhile, the Ru-CeO_2 catalyst prepared by a conventional coprecipitation method (2.4Ru-CeO_2-CP) also served as an important reference. More details on catalyst preparation can be found in Text S1.

2.2. Catalytic Performance Evaluation. Catalytic performance of the prepared Ru catalysts in C_3H_6 oxidation was evaluated on a fixed-bed quartz tube reactor. In each test, 60 mg of catalyst (40−60 mesh) mixed with 300 mg of SiC was loaded into the quartz tube reactor, and the feed gas (100 mL·min^{-1}) was composed of 4000 ppm C_3H_6, 5% O_2 and 5 vol % H_2O (when used), using Ar as balance, thus giving a weight hourly space velocity (WHSV) of 100,000 mL·g_{cat}^{-1}·h^{-1}. The outlet gas was analyzed by an online mass spectrometer, and the mass/charge (m/z) ratio used for the detection of C_3H_6 was 41. C_3H_6 conversion was calculated according to the following equation:

$$C_3H_6\ \text{conversion}\ (\%) = \left(\frac{[C_3H_6]_{in} - [C_3H_6]_{out}}{[C_3H_6]_{in}}\right) \times 100\%$$

The apparent activation energy (E_a) on the prepared catalysts in the C_3H_6 oxidation reaction was also measured. In a typical measurement, the mass ratio of catalysts to SiC was 1:20 and the C_3H_6 conversion was controlled below 20% to avoid possible heat and mass transfer effects. Reaction conditions: 4000 ppm C_3H_6, 5% O_2, Ar as balance, WHSV = 400,000 mL·g_{cat}^{-1}·h^{-1}.

2.3. Catalyst Characterization. The details of characterizations can be found in the Text S2.

https://doi.org/10.1021/acs.est.4c07159
Environ. Sci. Technol. 2024, 58, 19533−19544

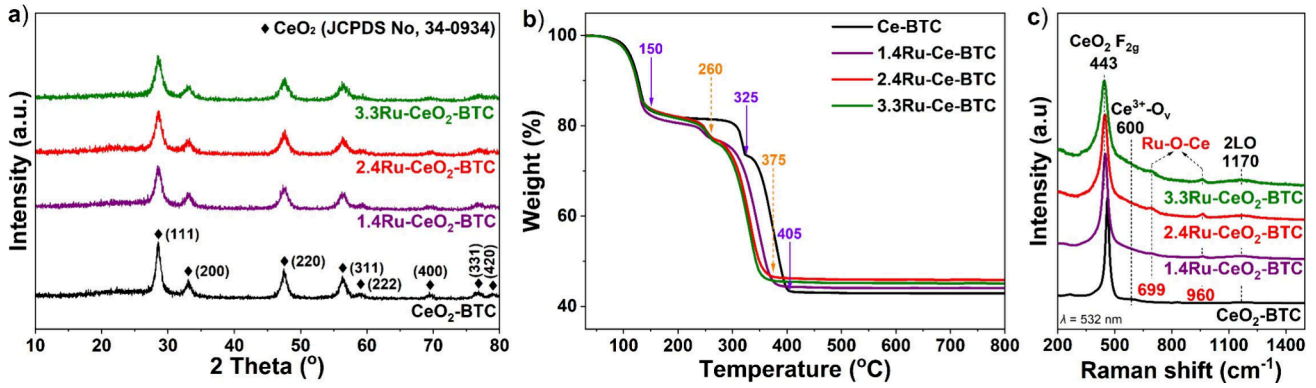

Figure 1. (a) XRD patterns for CeO_2-BTC and *x*Ru-CeO_2-BTC; (b) TG profiles for Ce-BTC and *x*Ru-Ce-BTC; and (c) Raman spectra for CeO_2-BTC and *x*Ru-CeO_2-BTC.

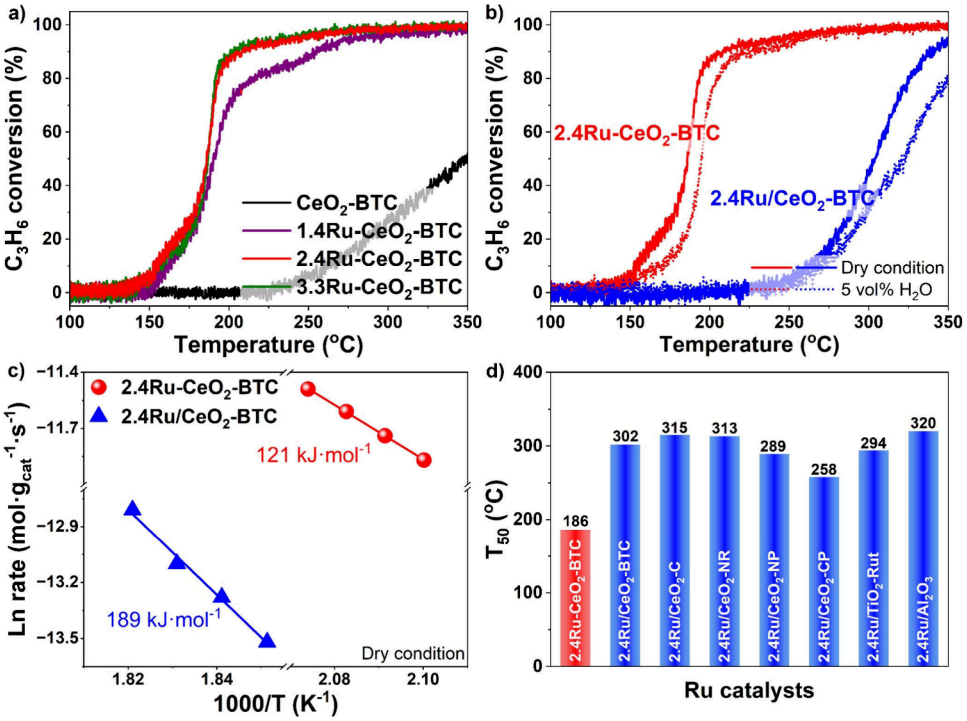

Figure 2. (a) C_3H_6 oxidation activity on CeO_2-BTC and *x*Ru-CeO_2-BTC. (b) C_3H_6 oxidation activity on 2.4Ru-CeO_2-BTC and 2.4Ru/CeO_2-BTC under dry and wet (5 vol % H_2O) conditions. Reaction condition: 4000 ppm C_3H_6, 5% O_2, 5% H_2O (when used), Ar as balance, WHSV = 100,000 $mL \cdot g_{cat}^{-1} \cdot h^{-1}$. (c) Apparent activation energy (E_a) on 2.4Ru-CeO_2-BTC and 2.4Ru/CeO_2-BTC in the C_3H_6 oxidation reaction measured under dry condition. (d) T_{50} for Ru catalysts in the C_3H_6 oxidation reaction.

3. RESULTS AND DISCUSSION

3.1. Structural Characterizations. In this work, a facile MOF-derived one-step hydrothermal method was employed to prepare *x*Ru-Ce-BTC materials with different Ru contents, which were further calcined in air at 450 °C to obtain *x*Ru-CeO_2-BTC catalysts (*x* in wt % was the actual Ru loading in *x*Ru-CeO_2-BTC, where *x* = 1.4, 2.4, and 3.3, and the catalyst without the addition of Ru was labeled as CeO_2-BTC).[37] As shown in Figure S1, the XRD peaks for Ce-BTC could be well indexed to a standard monoclinic Ce-BTC structure as reported elsewhere,[34,35] and *x*Ru-Ce-BTC catalysts exhibited similar XRD patterns as Ce-BTC, suggesting that the addition of Ru showed limited influence on the formation of the Ce-BTC structure. The SEM and EDS mapping images of the Ce-BTC and 2.4Ru-Ce-BTC catalysts were also collected to investigate their morphologies (Figure S2). It was observed that rod-like Ce-BTC and 2.4Ru-Ce-BTC were successfully synthesized, and the distribution of Ru matched well with that of Ce, suggesting the highly dispersed state of Ru. After pyrolysis, as shown in Figure 1a, XRD patterns for all *x*Ru-CeO_2-BTC catalysts could be attributed to the cubic fluorite type CeO_2 phase (JCPDS No. 34-0934), and no diffraction peaks assigned to Ce-BTC and crystalline Ru^0/RuO_x species were observed, suggesting the complete pyrolysis of Ce-BTC and the highly dispersed state of Ru species. Moreover, the intensity of the diffraction peaks for pure CeO_2-BTC decreased after the addition of Ru, suggesting that the doping of Ru species could suppress the crystallinity of CeO_2, probably due to the substitution of Ce^{4+} (0.97 Å) in CeO_2 by Ru ions with a smaller radius (<0.7 Å).[37]

TG technique is a powerful tool to investigate the thermal stability of catalysts. In this work, TG experiments were

https://doi.org/10.1021/acs.est.4c07159
Environ. Sci. Technol. 2024, 58, 19533−19544

conducted on Ce-BTC and *x*Ru-Ce-BTC to further confirm whether the complete pyrolysis of Ce-BTC species was achieved when the calcination temperature was 450 °C. As shown in Figure 1b, there were three distinct weight loss steps within the temperature range of 30−800 °C for Ce-BTC. The first weight loss step (step I) below 150 °C was related to the desorption of adsorbed or lattice-coordinated H_2O, the second weight loss step (step II) from 150 to 325 °C could be attributed to the desorption or oxidation of organic solvents, and the third weight loss step (step III) ending at 405 °C could be assigned to the combustion of the organic ligands.[8,34,39] Notably, after the addition of Ru, the ending temperature of step II (325 °C) and step III (405 °C) for Ce-BTC shifted to 260 and 375 °C, respectively, suggesting that the addition of Ru could effectively facilitate the pyrolysis of Ce-BTC at lower temperatures. The complete pyrolysis of Ce-BTC structures in Ce-BTC and *x*Ru-Ce-BTC catalysts could be achieved after the calcination at 450 °C in air, and the TG profiles for *x*Ru-CeO_2-BTC catalysts confirmed that no significant weight loss was observed within the temperature range of 100−800 °C (Figure S3).

Raman spectra for CeO_2-BTC and *x*Ru-CeO_2-BTC were collected to further investigate their structure (Figure 1c). For CeO_2-BTC, the bands at *ca.* 443, 600 and 1170 cm^{-1} could be assigned to the triply degenerate F_{2g} mode of the fluorite-type CeO_2 lattice, the defect-induced (D) mode originated from oxygen vacancies, and the second-order longitudinal optical (2LO) mode of the fluorite phase, respectively.[40] After the addition of Ru, a red-shift of the CeO_2 F_{2g} band was observed on *x*Ru-CeO_2-BTC catalysts (461 → 443 cm^{-1}), which could be resulted from the smaller lattice parameter of CeO_2 induced by Ru doping.[37,41] Moreover, two new bands at *ca.* 699 and 960 cm^{-1} emerged on *x*Ru-CeO_2-BTC, which were related to the formation of the Ru−O−Ce structure, suggesting the strong interaction between Ru and CeO_2.[13,16,42] The concentrations of the Ru−O−Ce structure ($I_{Ru-O-Ce}/I_{F_{2g}}$) and oxygen vacancy (O_v, $I_{D+2LO}/I_{F_{2g}}$) were also calculated and are listed in Table S1. A higher concentration of the Ru−O−Ce structure and O_v was achieved on 2.4Ru-CeO_2-BTC, which could be related to the formation of more Ru-CeO_2 interface on 2.4Ru-CeO_2-BTC.

3.2. C_3H_6 Oxidation Activity. C_3H_6 is one of the most common hydrocarbon pollutants emitted by vehicles and industries. Herein, C_3H_6 oxidation was used as a probe reaction to evaluate the catalytic oxidation performance of *x*Ru-CeO_2-BTC catalysts. As shown in Figure 2a, CeO_2-BTC exhibited negligible C_3H_6 oxidation activity from 100 to 350 °C. After the introduction of Ru, significantly improved catalytic performance was achieved on *x*Ru-CeO_2-BTC, with the T_{50} (the temperature at which C_3H_6 conversion reached 50%) on 1.4Ru-CeO_2-BTC decreased from 345 to 191 °C. With the further increase of Ru loading, C_3H_6 oxidation activity on *x*Ru-CeO_2-BTC increased slightly, and 2.4Ru-CeO_2-BTC exhibited comparable C_3H_6 oxidation activity to 3.3Ru-CeO_2-BTC. Therefore, it could be concluded that the optimal loading of Ru for *x*Ru-CeO_2-BTC catalysts in the C_3H_6 oxidation reaction was close to 2.4 wt %.

To further highlight the superiority of the one-step hydrothermal method in synthesizing highly efficient Ru catalysts for C_3H_6 oxidation, Ru supported on CeO_2-BTC prepared by a conventional incipient wetness impregnation (IWI) method was used as the reference catalyst. Surprisingly, 2.4Ru-CeO_2-BTC performed much better than 2.4Ru/CeO_2-BTC in the C_3H_6 oxidation reaction, implying that the one-step hydrothermal method showed a definite advantage over the conventional incipient wetness impregnation method in constructing highly efficient Ru sites for C_3H_6 oxidation (Figure 2b). The much lower apparent activation energy (E_a) on 2.4Ru-CeO_2-BTC (121 $kJ \cdot mol^{-1}$) than that on 2.4Ru/CeO_2-BTC (189 $kJ \cdot mol^{-1}$) in the C_3H_6 oxidation reaction further confirmed that 2.4Ru-CeO_2-BTC could better catalyze the oxidation of C_3H_6 than 2.4Ru/CeO_2-BTC (Figure 2c). Moreover, considering that H_2O in exhaust gas always shows a significant impact on the catalytic performance of various catalysts, C_3H_6 oxidation activity on 2.4Ru-CeO_2-BTC and 2.4Ru/CeO_2-BTC catalysts was also evaluated in the presence of 5 vol % H_2O (Figure 2b). Although both 2.4Ru-CeO_2-BTC and 2.4Ru/CeO_2-BTC suffered from deactivation due to the introduction of H_2O, 2.4Ru-CeO_2-BTC still showed much better C_3H_6 oxidation activity than 2.4Ru/CeO_2-BTC. The stability of 2.4Ru-CeO_2-BTC under dry and wet conditions was evaluated at 220 °C. It was found that the C_3H_6 oxidation activity on 2.4Ru-CeO_2-BTC showed a limited decrease during the test, indicating the superior stability of 2.4Ru-CeO_2-BTC (Figure S4). In addition, SO_2 was found to show a slight poisoning effect on 2.4Ru-CeO_2-BTC (Figure S5).

Furthermore, comparing to Ru catalysts supported on commercial CeO_2 support (2.4Ru/CeO_2-C), CeO_2 nanorod prepared by hydrothermal method (2.4Ru/CeO_2-NR), CeO_2 nanoparticles prepared by thermal decomposition of $Ce(NO_3)_3 \cdot 6H_2O$ (2.4Ru/CeO_2-NP), as well as a Ru-CeO_2 catalyst prepared by conventional coprecipitation method (2.4Ru-CeO_2-CP) and Ru catalysts supported on other widely used supports (2.4Ru/TiO_2-Rut and 2.4Ru/Al_2O_3), 2.4Ru-CeO_2-BTC still exhibited clear-cut advantages (Figure 2d and Figure S6), further verifying the superiority of the one-step hydrothermal method reported in this work. The specific surface area of the reference catalysts was also measured (Table S2). It was confirmed that the large specific surface area of 2.4Ru-CeO_2-BTC (109.7 $m^2 \cdot g^{-1}$) was not the key reason for its excellent C_3H_6 oxidation activity, as the specific surface area of 2.4Ru/Al_2O_3 (140.4 $m^2 \cdot g^{-1}$) and 2.4Ru/CeO_2-C (88.8 $m^2 \cdot g^{-1}$) with inferior catalytic performance was larger than, or at least close to that of 2.4Ru-CeO_2-BTC. Moreover, considering the cost of Ru/CeO_2 catalysts mainly came from the usage of Ru instead of Ce precursors, templates or precipitants, the 2.4Ru-CeO_2-BTC catalyst with much higher C_3H_6 oxidation activity would not show significant disadvantages in terms of price over Ru/CeO_2 catalysts prepared by conventional methods (Table S3). When compared with those recently reported PGMs catalysts for C_3H_6 oxidation, the 2.4Ru-CeO_2-BTC catalyst developed in this work still performed one of the best (Table S4). C_3H_8 oxidation activity on 2.4Ru-CeO_2-BTC and 2.4Ru/CeO_2-BTC was also evaluated to further investigate the potential of Ru catalysts developed in this work for hydrocarbon elimination (Figure S7). 2.4Ru-CeO_2-BTC still exhibited higher C_3H_8 oxidation activity than 2.4Ru/CeO_2-BTC, especially at the low temperature range.

3.3. Dispersion of Ru and Ru−O−Ce Structure. Considering that the dispersion of Ru might play a vital role in the catalytic oxidation of C_3H_6, various characterizations have been conducted to investigate the dispersion of Ru on 2.4Ru-CeO_2-BTC and 2.4Ru/CeO_2-BTC. SEM and EDS mapping images for all catalysts were first collected to investigate the morphologies of the catalysts and the

https://doi.org/10.1021/acs.est.4c07159
Environ. Sci. Technol. 2024, 58, 19533−19544

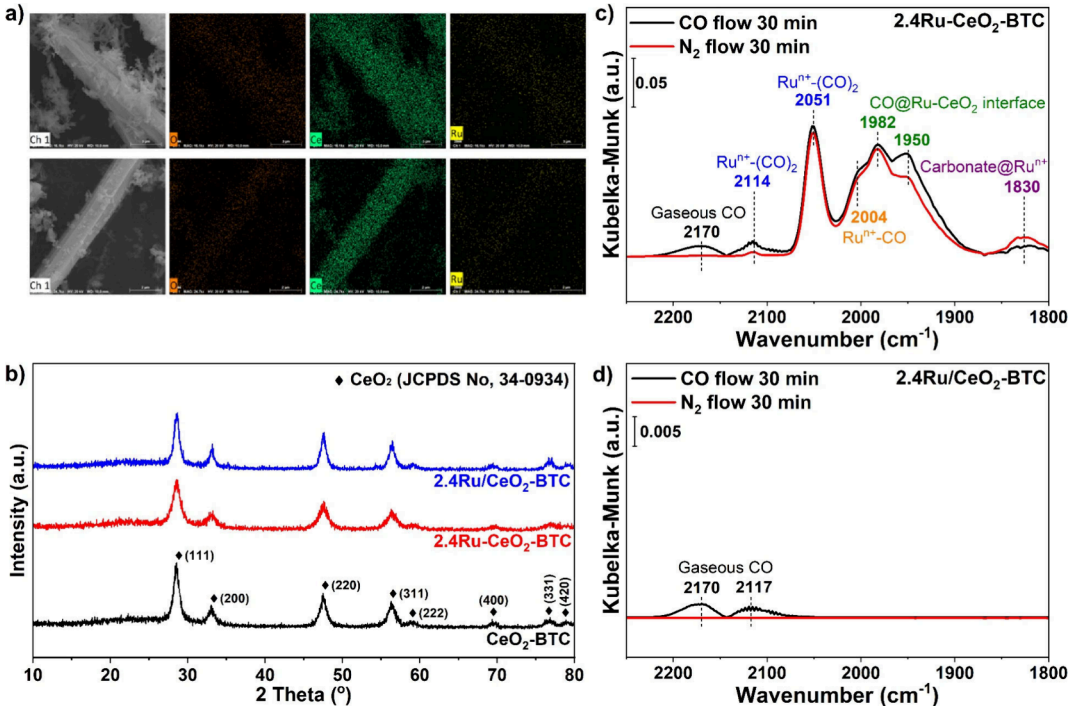

Figure 3. SEM and EDS mapping images for (a) 2.4Ru-CeO_2-BTC and 2.4Ru/CeO_2-BTC. (b) XRD patterns for CeO_2-BTC, 2.4Ru-CeO_2-BTC and 2.4Ru/CeO_2-BTC. *In situ* DRIFTS of CO adsorption on (c) 2.4Ru-CeO_2-BTC and (d) 2.4Ru/CeO_2-BTC at 30 °C.

distribution of Ru species (Figure S8 and Figures 3a and 3b). CeO_2-BTC, 2.4Ru-CeO_2-BTC and 2.4Ru/CeO_2-BTC were in rod-like morphology, the Ru species were highly dispersed without obvious aggregation on 2.4Ru-CeO_2-BTC and 2.4Ru/CeO_2-BTC, and the distribution of Ru species matched well with that of Ce. HR-TEM images of CeO_2-BTC, 2.4Ru-CeO_2-BTC and 2.4Ru/CeO_2-BTC were also collected (Figure S9). In addition to the lattice fringes with an interplanar spacing of 0.31 nm related to the (111) planes of fluorite type CeO_2 observed on all samples, the (110) planes of RuO_2 particles were also found on 2.4Ru/CeO_2-BTC, which were absent on 2.4Ru-CeO_2-BTC, suggesting that higher dispersion of Ru species might have been achieved on 2.4Ru-CeO_2-BTC. As shown in Figure 3b, all peaks in the XRD patterns for CeO_2-BTC, 2.4Ru-CeO_2-BTC and 2.4Ru/CeO_2-BTC could be assigned to CeO_2 with a cubic fluorite structure (JCPDS No. 34-0934), and no peak assigned to crystalline Ru or RuO_x species was observed on 2.4Ru-CeO_2-BTC and 2.4Ru/CeO_2-BTC, suggesting that Ru species were highly dispersed on these catalysts. Moreover, it was obvious that the full width at half-maximum (FWHM) of XRD peaks for 2.4Ru-CeO_2-BTC (0.69°) was wider than that for 2.4Ru/CeO_2-BTC (0.63°), suggesting the lower crystallinity of 2.4Ru-CeO_2-BTC, which could also be verified by the smaller crystalline size for 2.4Ru-CeO_2-BTC calculated according to the Scherrer equation (Table S5). N_2 physisorption isotherms and pore size distribution of CeO_2-BTC, 2.4Ru-CeO_2-BTC and 2.4Ru/CeO_2-BTC were also plotted and shown in Figure S10. It was found that all catalysts exhibited type IV isotherms with H3 hysteresis loops for N_2 adsorption−desorption, and the pore size distribution of all catalysts was similar, suggesting that the significant difference in the catalytic performance of 2.4Ru-CeO_2-BTC and 2.4Ru/CeO_2-BTC was not directly related to their pore structure.

To further investigate the dispersion states of Ru species within 2.4Ru-CeO_2-BTC and 2.4Ru/CeO_2-BTC catalysts, *in situ* DRIFTS of CO adsorption experiment was conducted (30 °C). As shown in Figure 3c, besides the bands at *ca.* 2171 and 2114 cm^{-1} assigned to gaseous CO, the well-defined bands at *ca.* 2051 and 2114 cm^{-1} observed on 2.4Ru-CeO_2-BTC could be assigned to dicarbonyl CO species adsorbed on highly dispersed Ru^{n+} sites (Ru^{n+}-$(CO)_2$).[33,37,43] As for those overlapping bands from 1900 to 2025 cm^{-1} on 2.4Ru-CeO_2-BTC, the band at *ca.* 2004 cm^{-1} could be ascribed to CO linearly adsorbed on Ru^{n+} sites (Ru^{n+}-CO),[17,44] and the bands at *ca.* 1982 and 1950 cm^{-1} were related to CO adsorbed on the Ru-CeO_2 interface (CO@Ru-CeO_2 interface).[15,45] In addition, the band at 1830 cm^{-1} could be attributed to carbonate species generated on Ru^{n+} species.[46] Inferred from the characteristics of the CO-IR bands on 2.4Ru-CeO_2-BTC, it could be concluded that the Ru species on it should be in the form of isolated Ru atoms or small RuO_x clusters with abundant Ru-CeO_2 interfacial sites. In clear contrast, only two bands related to gaseous CO were observed on 2.4Ru/CeO_2-BTC when exposed to CO flow (Figure 3d). After switching off CO and turning on the N_2 purge flow, no band could be observed within the range of 1800−2250 cm^{-1}, suggesting that Ru species on 2.4Ru/CeO_2-BTC were mainly in the form of Ru^0 or RuO_x nanoparticles, on which CO could be hardly adsorbed.[47−49] In short summary, Ru species on 2.4Ru-CeO_2-BTC and 2.4Ru/CeO_2-BTC were mainly in the form of isolated Ru ions/highly dispersed RuO_x clusters and larger Ru^0/RuO_x particles, respectively. The higher dispersion of Ru could also be determined by the results of XPS analysis (Table S6) that 2.4Ru-CeO_2-BTC (2.3%) possessed a higher surface concentration of Ru than 2.4Ru/CeO_2-BTC (1.1%).

Raman spectra for CeO_2-BTC, 2.4Ru-CeO_2-BTC and 2.4Ru/CeO_2-BTC were also collected to investigate the possible Ru−CeO_2 interaction and Ru−O−Ce structure on

https://doi.org/10.1021/acs.est.4c07159
Environ. Sci. Technol. 2024, 58, 19533−19544

Ru-CeO_2 catalysts. As shown in Figure 4a, comparing to CeO_2-BTC, a red-shift of the CeO_2 F_{2g} band was clearly observed on

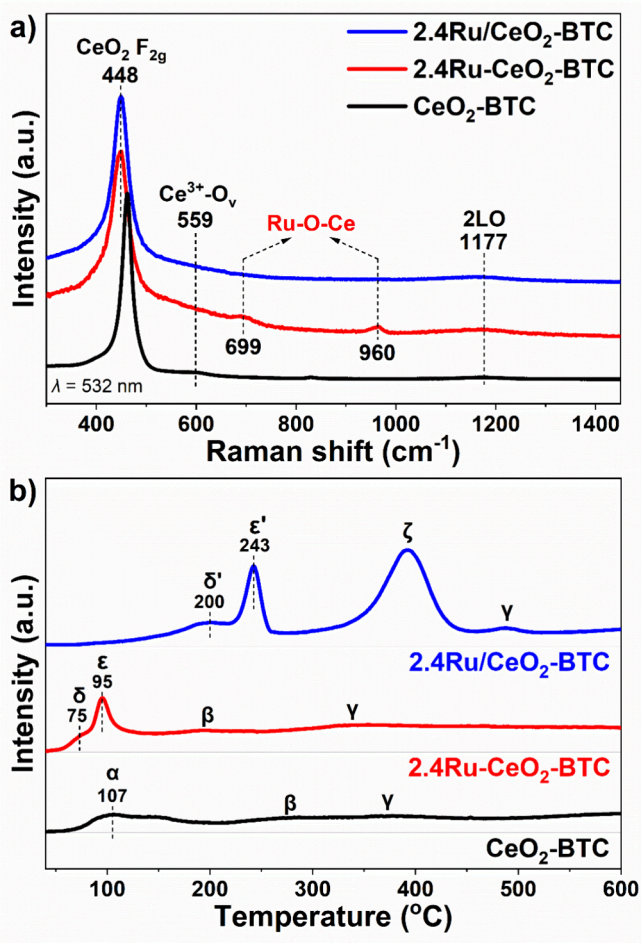

Figure 4. (a) Raman spectra and (b) CO-TPR profiles for CeO_2-BTC, 2.4Ru-CeO_2-BTC and 2.4Ru/CeO_2-BTC.

both 2.4Ru-CeO_2-BTC and 2.4Ru/CeO_2-BTC, probably due to the interaction between Ru and Ce.[17,50,51] Moreover, two distinct bands at *ca.* 699 and 960 cm^{-1} related to the Ru−O−Ce structure on 2.4Ru-CeO_2-BTC was hardly identified on 2.4Ru/CeO_2-BTC, and the peak area ratio of Ru−O−Ce bands ($I_{Ru-O-Ce}$) to CeO_2 F_{2g} bands ($I_{F_{2g}}$), i.e., $I_{Ru-O-Ce}/I_{F_{2g}}$, was calculated to compare the relative concentration of the Ru−O−Ce structure on Ru/CeO_2 catalysts (Table S6).[37] It was found that a higher concentration of Ru−O−Ce structure was generated on 2.4Ru-CeO_2-BTC than 2.4Ru/CeO_2-BTC, suggesting that the one-step hydrothermal method could better facilitate the dispersion of Ru species, thus generating more Ru−O−Ce linkages and stronger Ru−CeO_2 interaction. Such a significant difference in the concentration of Ru−O−Ce structure might be the main reason for the different catalytic performance of 2.4Ru-CeO_2-BTC and 2.4Ru/CeO_2-BTC in the C_3H_6 oxidation reaction. The relative concentration of oxygen vacancies ($(I_{D+2LO})/I_{F_{2g}}$) on Ru/CeO_2 catalysts was also calculated and listed in Table S6.[13,16] The formation of more oxygen vacancies on 2.4Ru-CeO_2-BTC (28.2%) compared to CeO_2-BTC (9.1%) and 2.4Ru/CeO_2-BTC (19.9%) suggested that the introduction of Ru via one-step hydrothermal method could induce the formation of more oxygen vacancies, which might be related to the surface lattice distortion caused by the incorporation of Ru into the surface lattice of the CeO_2 support.

Besides being used to evaluate the redox performance of catalysts, the TPR technique was also a powerful tool to investigate the interaction between metal (oxide) active sites and supports. In this work, CO-TPR experiment was conducted and CO-TPR profiles were plotted in Figure 4b. There were three CO-consumption peaks (α, β and γ) observed on CeO_2-BTC, which could be assigned to the reaction between CO and surface active chemisorbed oxygen species (α), the reduction of surface Ce^{4+}/mobile lattice oxygen (β), and the reduction of bulk CeO_2 (γ), respectively.[23,33,41] For 2.4Ru-CeO_2-BTC, in addition to peaks β and γ attributed to the reduction of surface Ce^{4+} and bulk CeO_2, new CO consumption peaks centered at 75 (δ) and 95 °C (ε) were also observed, which could be assigned to the reduction of Ru−O and Ru−O−Ce structures, respectively.[42,44] Interestingly, the CO-TPR profile for 2.4Ru/CeO_2-BTC showed different features compared to those for CeO_2-BTC and 2.4Ru-CeO_2-BTC. Specifically, CO-consumption peaks at 200 (δ') and 243 °C (ε') should be related to the reduction of RuO_x particles and the reduction of surface Ce^{4+} and partial mobile lattice oxygen species, respectively.[13] Remarkably, an intensive CO-consumption peak at *ca.* 390 °C (ζ) was also observed on 2.4Ru/CeO_2-BTC. Considering that RuO_x nanoparticles on 2.4Ru/CeO_2-BTC have been reduced by CO below 300 °C, this intensive-CO consumption peak should be related to the "reverse oxygen spillover effect".[47−49] That is, Ru particles on CeO_2 could induce the migration of subsurface and bulk oxygen species to the surface of CeO_2 and then react with CO. Although the total CO consumption for 2.4Ru/CeO_2-BTC was comparable to that for 2.4Ru-CeO_2-BTC (Table S7), the dramatic reverse oxygen spillover on 2.4Ru/CeO_2-BTC occurred at high temperatures (>300 °C) could hardly contribute to the low temperature C_3H_6 oxidation, whereas the Ru−O−Ce structure on 2.4Ru-CeO_2-BTC with superior low temperature redox performance might play a key role in catalyzing the oxidation of C_3H_6 at low temperatures. The conclusions drawn by CO-TPR were also well supported by the results of H_2-TPR (Figure S11).

3.4. Surface Chemical States and Coordination Environment of Ru. Based on the results of *in situ* DRIFTS of CO adsorption, Raman spectra and CO-TPR, it could be deduced that Ru species with different dispersion and Ru−CeO_2 interaction on 2.4Ru/CeO_2-BTC and 2.4Ru-CeO_2-BTC should exist in different states. Due to the overlap of Ru 3d XPS and C 1s XPS, as well as the rather low intensity of Ru 3p XPS, XAS analysis instead of XPS analysis was applied to determine the valence and dispersion of Ru species on 2.4Ru/CeO_2-BTC and 2.4Ru-CeO_2-BTC.[52] As shown in Figure 5a, the white line intensities of the Ru K edge X-ray absorption near-edge structure (XANES) for 2.4Ru/CeO_2-BTC and 2.4Ru-CeO_2-BTC were both similar to that for RuO_2, suggesting that Ru species on those two catalysts were mainly in the form of Ru^{4+}. The results of XANES linear combination fitting analysis further confirmed that the average valence of Ru species on both 2.4Ru/CeO_2-BTC (3.92 ± 0.02) and 2.4Ru-CeO_2-BTC (3.67 ± 0.03) was close to +4 (Figure S12 and Table S8). To investigate the local coordination environment and dispersion of Ru species, X-ray absorption near-edge structure (EXAFS) curve fitting analysis was conducted

https://doi.org/10.1021/acs.est.4c07159
Environ. Sci. Technol. 2024, 58, 19533−19544

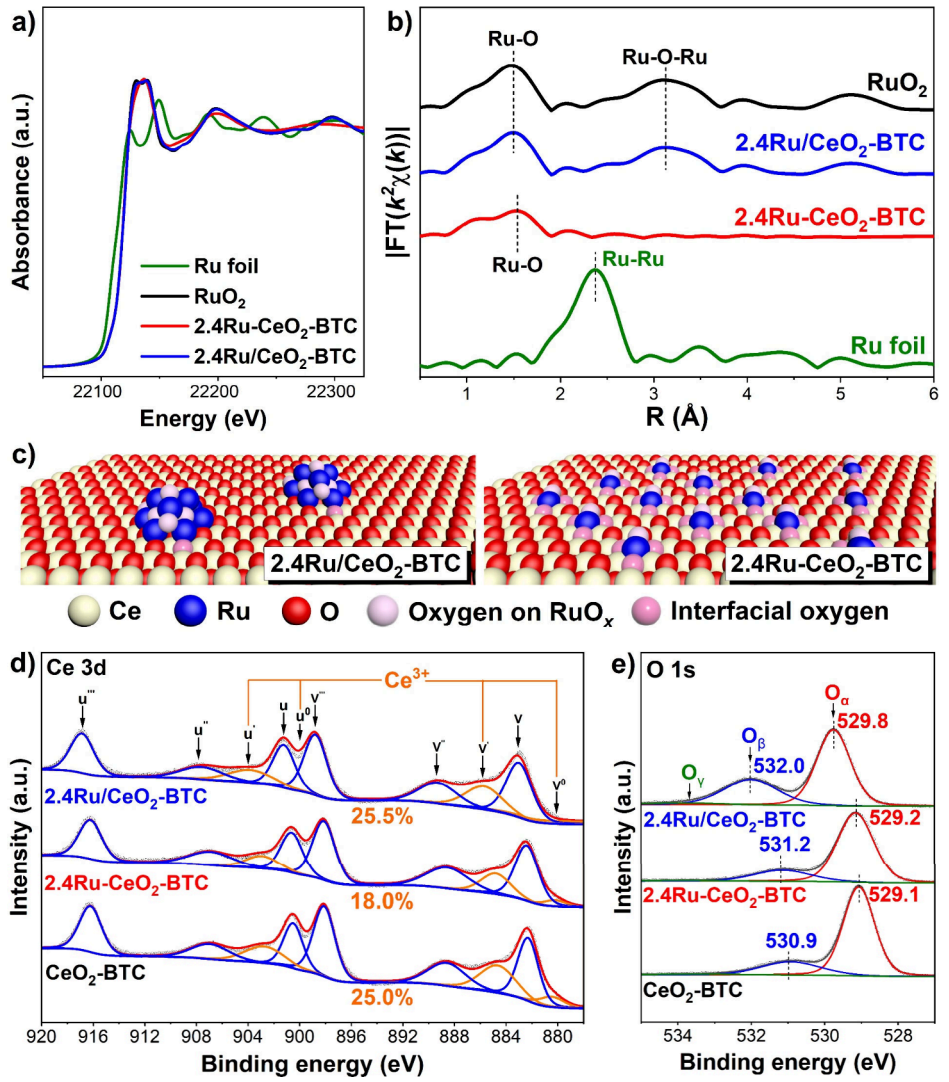

Figure 5. (a) Normalized Ru K edge XANES and (b) Fourier transformed k^2-weighted EXAFS oscillations in R space for Ru K edge in Ru foil, RuO_2, 2.4Ru-CeO_2-BTC, and 2.4Ru/CeO_2-BTC. (c) Surface structural models for 2.4Ru/CeO_2-BTC (left) and 2.4Ru-CeO_2-BTC (right). (d) Ce 3d and (e) O 1s XPS for CeO_2-BTC, 2.4Ru-CeO_2-BTC and 2.4Ru/CeO_2-BTC.

(Figure 5b and Figure S13). For 2.4Ru/CeO_2-BTC, the presence of Ru−O and Ru−O−Ru shells and the absence of the Ru−Ru shell in its EXAFS curve suggested that Ru species on 2.4Ru/CeO_2-BTC have agglomerated into RuO_x particles. Besides, the quite close coordination number of Ru−O and Ru−O−Ru shells on 2.4Ru/CeO_2-BTC compared to those on RuO_2 reference further confirmed the formation of RuO_2 particles on 2.4Ru/CeO_2-BTC (Table S9). Differently, both Ru−O−Ru and Ru−Ru shells were absent on 2.4Ru-CeO_2-BTC, indicating that the Ru species on it were dominantly in the form of single atoms. The relatively longer Ru−O bond in 2.4Ru-CeO_2-BTC (2.00 ± 0.02 Å) than that in 2.4Ru/CeO_2-BTC and RuO_2 (1.97 ± 0.02 Å) suggested that Ru ions might have been incorporated into the surface lattice of the CeO_2 support. When combining the results of *in situ* DRIFTS of CO adsorption, HR-TEM, Raman spectra and XAS, it could be concluded that Ru species on 2.4Ru/CeO_2-BTC and 2.4Ru-CeO_2-BTC were in the form of RuO_2 particles and Ru single atoms, respectively. The proposed surface structures of 2.4Ru/CeO_2-BTC and 2.4Ru-CeO_2-BTC have been illustrated in Figure 5c.

Although XPS was not a powerful tool for revealing the valence states of Ru species on supported catalysts, it still could effectively elucidate the chemical states of Ce and oxygen species (Figures 5d and 5e and Table S6). According to the deconvolution results of Ce 3d XPS, the ratio of surface Ce^{3+} species in total Ce species (i.e., $Ce^{3+}/(Ce^{3+} + Ce^{4+})$ for CeO_2-BTC was *ca.* 25.0%. It was interesting to see that 2.4Ru-CeO_2-BTC showed a lower ratio of Ce^{3+} (18.0%) than CeO_2-BTC,[31,41] probably due to the oxidation of Ce^{3+} induced by highly dispersed Ru ions during the calcination process. For 2.4Ru/CeO_2-BTC, the ratio of surface Ce^{3+} on it (25.5%) was comparable to that on CeO_2-BTC (25.0%), well corroborating the weak Ru−CeO_2 interaction. As for the O 1s XPS, peak O_α, peak O_β and peak O_γ were assigned to the lattice oxygen species, surface adsorbed oxygen species and surface hydroxyl groups, respectively.[16,46] The relative concentrations of surface oxygen species $((O_\beta + O_\gamma)/(O_\alpha + O_\beta + O_\gamma))$ were calculated and listed in Table S6. It was found that much more surface oxygen species were formed on 2.4Ru/CeO_2-BTC (37.0%) than CeO_2-BTC (24.5%) and 2.4Ru-CeO_2-BTC (21.8%). Based on the results of CO-TPR and *in situ* DRIFTS of CO adsorption, it could be inferred that oxygen species on RuO_2

https://doi.org/10.1021/acs.est.4c07159
Environ. Sci. Technol. 2024, 58, 19533−19544

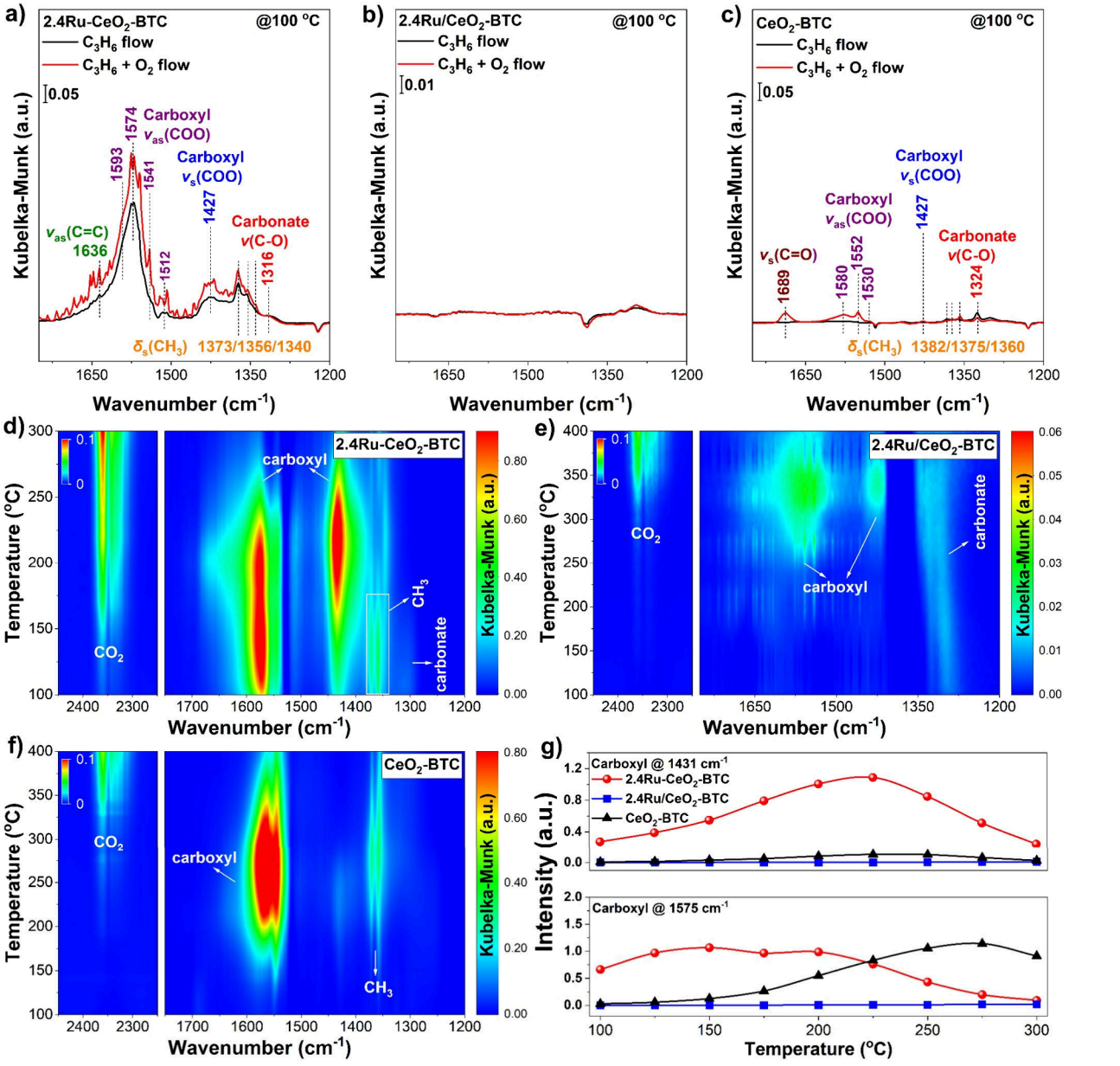

Figure 6. *In situ* DRIFTS of C_3H_6 adsorption and oxidation at 100 °C on (a) 2.4Ru-CeO_2-BTC, (b) 2.4Ru/CeO_2-BTC and (c) CeO_2-BTC. *In situ* DRIFTS of C_3H_6 oxidation from 100 to 400 °C on (d) 2.4Ru-CeO_2-BTC, (e) 2.4Ru/CeO_2-BTC and (f) CeO_2-BTC. (g) The intensity of the bands assigned to carboxyl species (1431 and 1575 cm^{-1}) as a function of reaction temperature during the *in situ* DRIFTS of C_3H_6 oxidation.

particles (2.4Ru/CeO_2-BTC) were recognized as surface oxygen species, while oxygen species coordinated to highly dispersed Ru species (2.4Ru-CeO_2-BTC) were recognized as lattice oxygen species in the surface lattice of CeO_2. Such significant difference further indicated that highly dispersed Ru species on 2.4Ru-CeO_2-BTC have incorporated into the surface lattice of the CeO_2-BTC support and abundant Ru^{4+}−O−Ce^{4+} structures have been generated.

3.5. Reaction Mechanism. To in-depth reveal the intrinsic reasons for the higher C_3H_6 oxidation activity on 2.4Ru-CeO_2-BTC, systematic *in situ* DRIFTS experiments of C_3H_6 adsorption and oxidation were performed. As shown in Figure 6a, when C_3H_6 flow was introduced to 2.4Ru-CeO_2-BTC, several bands assigned to carboxyl and carbonate species were observed (1200−1750 cm^{-1}) on 2.4Ru-CeO_2-BTC.[16,41] The bands at *ca.* 1427 and 1500−1600 cm^{-1} could be attributed to carboxyl species.[41,53,54] The bands at about 1320 cm^{-1} could be assigned to ν(C−O) in carbonate species.[55,56] The bands at 1340−1390 and 1636 cm^{-1} could be assigned to $\delta_s(CH_3)$ and ν_{as}(C=C), respectively.[14,54] The formation of oxygenated species indicated that C_3H_6 could be effectively adsorbed on 2.4Ru-CeO_2-BTC and further react with the active surface oxygen species. Nevertheless, there was no intensive band emerging on 2.4Ru/CeO_2-BTC and CeO_2-BTC (Figures 6b and 6c), suggesting that C_3H_6 was hardly adsorbed on them, or surface oxygen species on them were inert to react with C_3H_6 to form intermediates (e.g., carboxyl species and carbonates, *etc.*) at low temperature (≤100 °C). Such a phenomenon was highly consistent with the results of CO-TPR that oxygen species in the Ru−O or Ru−O−Ce structure on 2.4Ru-CeO_2-BTC were highly reactive at low temperatures, while 2.4Ru/CeO_2-BTC exhibited poor low temperature redox

https://doi.org/10.1021/acs.est.4c07159
Environ. Sci. Technol. 2024, 58, 19533−19544

performance. Furthermore, upon the introduction of O_2 to the feed stream, an enhancement in the intensity of these bands assigned to carboxyl and carbonate species on 2.4Ru-CeO_2-BTC was observed. In clear contrast, limited additional intermediate species were formed on 2.4Ru/CeO_2-BTC and CeO_2-BTC, further suggesting that O_2 could be activated more effectively on the 2.4Ru-CeO_2-BTC catalyst to react with C_3H_6 and facilitate the formation of intermediate species.

To further monitor the reaction process of C_3H_6 oxidation on Ru catalysts, *in situ* DRIFTS of C_3H_6 oxidation under continuous heating conditions (2 °C·min^{-1}) was conducted (Figures 6d−6g). For 2.4Ru-CeO_2-BTC (Figure 6d), a group of intensive bands assigned to carboxyl species (1530−1620 cm^{-1}) were observed at 100 °C. Besides, three groups of relatively weak bands attributed to carboxyl species (1380−1460 cm^{-1}), $\delta_s(CH_3)$ modes (1350−1380 cm^{-1}) and carbonate species (1270−1350 cm^{-1}) were also observed. The intensity of the IR bands attributed to carboxyl species and gaseous CO_2 as a function of reaction temperature was plotted and shown in Figure 6g and Figure S14 for a better understanding of the results of the DRIFTS study. For 2.4Ru-CeO_2-BTC, combined with the fact that the boost in C_3H_6 oxidation activity on 2.4Ru-CeO_2-BTC at *ca.* 225 °C was accompanied by the significant decrease in the intensity of IR bands at 1431 and 1575 cm^{-1} attributed to carboxyl species and the increase in the intensity of IR band of gaseous CO_2 (2300−2400 cm^{-1}), it was confirmed that the facile decomposition/desorption of carboxyl species was directly related to the superior C_3H_6 oxidation activity on 2.4Ru-CeO_2-BTC. As shown in Figure 6e, carboxyl species (1530−1620 and 1380−1460 cm^{-1}) were observed on 2.4Ru/CeO_2-BTC catalysts at higher temperatures (>300 °C), which was probably due to the inferior low temperature redox performance of 2.4Ru/CeO_2-BTC. However, only one group of bands attributed to carboxyl species (1530−1620 cm^{-1}) emerged on CeO_2-BTC throughout the experiment (Figure 6f), suggesting that the carboxyl species at 1530−1620 cm^{-1} was related to Ce sites, and the bands at 1380−1460 cm^{-1} could be the carboxyl species adsorbed on Ru sites. Migration of carboxyl species from Ce sites to Ru sites could occur at relatively high temperatures, especially on 2.4Ru-CeO_2-BTC. Even though the temperature at which carboxyl species were formed on CeO_2-BTC was lower than that on 2.4Ru/CeO_2-BTC, 2.4Ru/CeO_2-BTC still exhibited better activity than CeO_2-BTC, indicating the critical role of Ru sites in facilitating the decomposition and desorption of carboxyl species on Ru-CeO_2 catalysts. That is, the exposure of more Ru sites on 2.4Ru-CeO_2-BTC with higher Ru dispersion would also contribute to its higher C_3H_6 oxidation activity.

4. ENVIRONMENTAL IMPLICATIONS

Ru/CeO_2 catalysts have been intensively investigated in the environmental catalysis field due to their superior performance in the catalytic oxidation of VOCs. Determination of the most reactive sites on Ru/CeO_2 catalysts played a pivotal role in the design of efficient catalysts for VOCs elimination. In this work, starting from the construction of Ru/CeO_2 with distinct Ru dispersions via facile methods, it was disclosed for the first time that highly dispersed Ru species on CeO_2 with the formation of abundant Ru−O−Ce linkages were the more reactive sites for the catalytic oxidation of C_3H_6. Besides, the importance of active oxygen species in the Ru−O−Ce structure and Ru sites in facilitating the formation, decomposition and desorption of intermediates was also highlighted. It is believed that the findings of this work can provide valuable guidance for developing highly efficient Ru/CeO_2 catalysts for VOCs elimination and contribute to the environmental catalysis community.

■ ASSOCIATED CONTENT

Supporting Information

The Supporting Information is available free of charge at https://pubs.acs.org/doi/10.1021/acs.est.4c07159.

Details of catalyst preparation and characterizations, results of N_2 physisorption, XRD, Raman spectra, XPS, CO-TPR, SEM and EDS mapping images, TG profiles, stability test, C_3H_6 oxidation activity, HR-TEM images, and XAS analysis (PDF)

■ AUTHOR INFORMATION

Corresponding Authors

Fudong Liu − *Department of Chemical and Environmental Engineering, Bourns College of Engineering, Center for Environmental Research and Technology (CE-CERT), Materials Science and Engineering (MSE) Program, University of California, Riverside, California 92521, United States;* orcid.org/0000-0001-8771-5938; Email: fudong.liu@ucr.edu, lfd1982@gmail.com

Wei Tan − *State Key Laboratory of Pollution Control and Resource Reuse, School of Environment, Jiangsu Key Laboratory of Vehicle Emissions Control, Center of Modern Analysis, Key Laboratory of Mesoscopic Chemistry of MOE, School of Chemistry and Chemical Engineering, Nanjing University, Nanjing 210023, China;* orcid.org/0000-0002-1481-9346; Email: tanwei@nju.edu.cn

Authors

Bifeng Zhang − *State Key Laboratory of Pollution Control and Resource Reuse, School of Environment, Jiangsu Key Laboratory of Vehicle Emissions Control, Center of Modern Analysis, Key Laboratory of Mesoscopic Chemistry of MOE, School of Chemistry and Chemical Engineering, Nanjing University, Nanjing 210023, China*

Jiawei Yang − *State Key Laboratory of Pollution Control and Resource Reuse, School of Environment, Jiangsu Key Laboratory of Vehicle Emissions Control, Center of Modern Analysis, Key Laboratory of Mesoscopic Chemistry of MOE, School of Chemistry and Chemical Engineering, Nanjing University, Nanjing 210023, China*

Yibo Mu − *State Key Laboratory of Pollution Control and Resource Reuse, School of Environment, Jiangsu Key Laboratory of Vehicle Emissions Control, Center of Modern Analysis, Key Laboratory of Mesoscopic Chemistry of MOE, School of Chemistry and Chemical Engineering, Nanjing University, Nanjing 210023, China*

Xiaoyu Ji − *State Key Laboratory of Pollution Control and Resource Reuse, School of Environment, Jiangsu Key Laboratory of Vehicle Emissions Control, Center of Modern Analysis, Key Laboratory of Mesoscopic Chemistry of MOE, School of Chemistry and Chemical Engineering, Nanjing University, Nanjing 210023, China*

Yandi Cai − *State Key Laboratory of Pollution Control and Resource Reuse, School of Environment, Jiangsu Key Laboratory of Vehicle Emissions Control, Center of Modern Analysis, Key Laboratory of Mesoscopic Chemistry of MOE,*

https://doi.org/10.1021/acs.est.4c07159
Environ. Sci. Technol. 2024, 58, 19533−19544

School of Chemistry and Chemical Engineering, Nanjing University, Nanjing 210023, China

Nan Jiang − *State Key Laboratory of Pollution Control and Resource Reuse, School of Environment, Jiangsu Key Laboratory of Vehicle Emissions Control, Center of Modern Analysis, Key Laboratory of Mesoscopic Chemistry of MOE, School of Chemistry and Chemical Engineering, Nanjing University, Nanjing 210023, China*

Shaohua Xie − *Department of Chemical and Environmental Engineering, Bourns College of Engineering, Center for Environmental Research and Technology (CE-CERT), Materials Science and Engineering (MSE) Program, University of California, Riverside, California 92521, United States*

Qiuhui Qian − *National and Local Joint Engineering Laboratory of Municipal Sewage Resource Utilization Technology, School of Environmental Science and Engineering, Suzhou University of Science and Technology, Suzhou 215009, China*

Lin Dong − *State Key Laboratory of Pollution Control and Resource Reuse, School of Environment, Jiangsu Key Laboratory of Vehicle Emissions Control, Center of Modern Analysis, Key Laboratory of Mesoscopic Chemistry of MOE, School of Chemistry and Chemical Engineering, Nanjing University, Nanjing 210023, China;* orcid.org/0000-0002-8393-6669

Complete contact information is available at: https://pubs.acs.org/10.1021/acs.est.4c07159

Notes

The authors declare no competing financial interest.

■ ACKNOWLEDGMENTS

W.T. thanks the support from National Natural Science Foundation of China (22306090), the Natural Science Foundation of Jiangsu Province (BK20230773), the Young Elite Scientists Sponsorship Program by CAST (YESS20230298), the China Postdoctoral Science Foundation (2024M751391 and GZB20240304), and the Jiangsu Funding Program for Excellent Postdoctoral Talent (2024ZB828). L.D. thanks the support from the National Natural Science Foundation of China (22272077) and the Natural Science Foundation of Jiangsu Province (BK20231513). F.L. thanks the Startup Fund from the University of California, Riverside (UCR) and the NSF Grant (CHE-1955343). This research used beamline 7-BM (QAS) of the National Synchrotron Light Source II, a U.S. Department of Energy (DOE) Office of Science User Facility operated for the DOE Office of Science by Brookhaven National Laboratory under Contract DE-SC0012704. F.L. sincerely thanks Dr. Lu Ma and Dr. Steven N. Ehrlich for the support in XAS measurements.

■ REFERENCES

(1) Lewis, A. C.; Carslaw, N.; Marriott, P. J.; Kinghorn, R. M.; Morrison, P.; Lee, A. L.; Bartle, K. D.; Pilling, M. J. A larger pool of Ozone-Forming Carbon Compounds in Urban Atmospheres. *Nature* **2000**, *405*, 778−781.

(2) Atkinson, R.; Arey, J. Atmospheric Degradation of Volatile Organic Compounds. *Chem. Rev.* **2003**, *103*, 4605−4638.

(3) Domeno, C.; Rodriguez-Lafuente, A.; Martos, J.; Bilbao, R.; Nerin, C. VOC Removal and Deodorization of Effluent Gases from an Industrial Plant by Photo-Oxidation, Chemical Oxidation, and Ozonization. *Environ. Sci. Technol.* **2010**, *44*, 2585−2591.

(4) Datye, A. K.; Votsmeier, M. Opportunities and Challenges in the Development of Advanced Materials for Emission Control Catalysts. *Nat. Mater.* **2021**, *20*, 1049−1059.

(5) Huang, H. J.; Yu, D. S.; Hu, F.; Huang, S. C.; Song, J. N.; Chen, H. Y.; Li, L. L.; Peng, S. J. Clusters Induced Electron Redistribution to Tune Oxygen Reduction Activity of Transition Metal Single-Atom for Metal-Air Batteries. *Angew. Chem., Int. Ed.* **2022**, *61*, No. e202116068.

(6) Aouad, S.; Abi-Aad, E.; Aboukais, A. Simultaneous Oxidation of Carbon Black and Volatile Organic Compounds over Ru/CeO_2 Catalysts. *Appl. Catal., B* **2009**, *88*, 249−256.

(7) Xiong, H. F.; Wiebenga, M. H.; Carrillo, C.; Gaudet, J. R.; Pham, H. N.; Kunwar, D.; Oh, S. H.; Qi, G. S.; Kim, C. H.; Datye, A. K. Design Considerations for Low-Temperature Hydrocarbon Oxidation Reactions on Pd Based Catalysts. *Appl. Catal., B* **2018**, *236*, 436−444.

(8) Jeong, H.; Kwon, O.; Kim, B.-S.; Bae, J.; Shin, S.; Kim, H. E.; Kim, J.; Lee, H. Highly Durable Metal Ensemble Catalysts with Full Dispersion for Automotive Applications beyond Single-Atom Catalysts. *Nat. Catal.* **2020**, *3*, 368−375.

(9) Tan, W.; Alsenani, H.; Xie, S. H.; Cai, Y. D.; Xu, P.; Liu, A. N.; Ji, J. W.; Gao, F.; Dong, L.; Chukwu, E.; Yang, M.; Liu, F. D. Tuning Single-atom Pt_1-CeO_2 Catalyst for Efficient CO and C_3H_6 Oxidation: Size Effect of Ceria on Pt Structural Evolution. *ChemNanoMat* **2020**, *6*, 1797−1805.

(10) Cen, B. H.; Tang, C.; Lu, J. Q.; Chen, J.; Luo, M. F. Different Roles of MoO_3 and Nb_2O_5 Promotion in Short-Chain Alkane Combustion over Pt/ZrO_2 Catalysts. *Chin. J. Catal.* **2021**, *42*, 2287−2295.

(11) Xie, S.; Wang, Z.; Tan, W.; Zhu, Y.; Collier, S.; Ma, L.; Ehrlich, S. N.; Xu, P.; Yan, Y.; Xu, T.; Deng, J.; Liu, F. Highly Active and Stable Palladium Catalysts on Novel Ceria-Alumina Supports for Efficient Oxidation of Carbon Monoxide and Hydrocarbons. *Environ. Sci. Technol.* **2021**, *55*, 7624−7633.

(12) Wang, Z.; Wang, W.; Khalid, O.; Weber, T.; Spriewald Luciano, A.; Zhan, W.; Smarsly, B. M.; Over, H. Supported $Ru_xIr_{1-x}O_2$ Mixed Oxides Catalysts for Propane Combustion: Resistance Against Water Poisoning. *ChemCatChem.* **2022**, *14*, No. e202200149.

(13) Huang, H.; Dai, Q. G.; Wang, X. Y. Morphology Effect of Ru/CeO_2 Catalysts for the Catalytic Combustion of Chlorobenzene. *Appl. Catal., B* **2014**, *158*−*159*, 96−105.

(14) Hu, Z.; Wang, Z.; Guo, Y.; Wang, L.; Guo, Y. L.; Zhang, J. S.; Zhan, W. C. Total Oxidation of Propane over a Ru/CeO_2 Catalyst at Low Temperature. *Environ. Sci. Technol.* **2018**, *52*, 9531−9541.

(15) Li, J. H.; Liu, Z. Q.; Cullen, D. A.; Hu, W. H.; Huang, J.; Yao, L.; Peng, Z. M.; Liao, P. L.; Wang, R. g. Distribution and Valence State of Ru Species on CeO_2 Supports: Support Shape Effect and Its Influence on CO Oxidation. *ACS Catal.* **2019**, *9*, 11088−11103.

(16) Wang, Z.; Huang, Z. P.; Brosnahan, J. T.; Zhang, S.; Guo, Y. L.; Guo, Y.; Wang, L.; Wang, Y. S.; Zhan, W. C. Ru/CeO_2 Catalyst with Optimized CeO_2 Support Morphology and Surface Facets for Propane Combustion. *Environ. Sci. Technol.* **2019**, *53*, 5349−5358.

(17) Qin, X. X.; Chen, M.; Chen, X. Y.; Zhang, J. H.; Wang, X. X.; Fang, J. H.; Zhang, C. B. Effects of the Metal-Support Interaction in Ru/CeO_2 Nanostructures on Active Oxygen Species for HCHO/CO Oxidation. *ACS Appl. Nano Mater.* **2022**, *5*, 15574−15582.

(18) Ganzler, A. M.; Casapu, M.; Vernoux, P.; Loridant, S.; Cadete Santos Aires, F. J.; Epicier, T.; Betz, B.; Hoyer, R.; Grunwaldt, J.-D. Tuning the Structure of Platinum Particles on Ceria In Situ for Enhancing the Catalytic Performance of Exhaust Gas Catalysts. *Angew. Chem., Int. Ed.* **2017**, *56*, 13078−13082.

(19) Gänzler, A. M.; Casapu, M.; Maurer, F.; Störmer, H.; Gerthsen, D.; Ferre, G. r.; Vernoux, P.; Bornmann, B.; Frahm, R.; Murzin, V.; Nachtegaal, M.; Votsmeier, M.; Grunwaldt, J. D. Tuning the Pt/CeO_2 Interface by in Situ Variation of the Pt Particle Size. *ACS Catal.* **2018**, *8*, 4800−4811.

(20) Ma, J.; Lou, Y.; Cai, Y. F.; Zhao, Z. Y.; Wang, L.; Zhan, W. C.; Guo, Y. L.; Guo, Y. The Relationship between the Chemical State of Pd Species and the Catalytic Activity for Methane Combustion on Pd/CeO_2. *Catal. Sci. Technol.* **2018**, *8*, 2567−2577.

(21) Chen, S. Y.; Li, S. D.; You, R. Y.; Guo, Z.; Wang, F.; Li, G. X.; Yuan, W. T.; Zhu, B. E.; Gao, Y.; Zhang, Z.; Yang, H. S.; Wang, Y. Elucidation of Active Sites for CH_4 Catalytic Oxidation over Pd/CeO_2 Via Tailoring Metal-Support Interactions. *ACS Catal.* **2021**, *11*, 5666−5677.
(22) Tan, W.; Xie, S.; Le, D.; Diao, W.; Wang, M.; Low, K.-B.; Austin, D.; Hong, S.; Gao, F.; Dong, L.; Ma, L.; Ehrlich, S. N.; Rahman, T. S.; Liu, F. Fine-Tuned Local Coordination Environment of Pt Single Atoms on Ceria Controls Catalytic Reactivity. *Nat. Commun.* **2022**, *13*, 7070.
(23) Tan, W.; Cai, Y. D.; Yu, H. W.; Xie, S. H.; Wang, M. Y.; Ye, K. L.; Ma, L.; Ehrlich, S. N.; Gao, F.; Dong, L.; Liu, F. D. Tuning the Interaction between Platinum Single Atoms and Ceria by Zirconia Doping for Efficient Catalytic Ammonia Oxidation. *Environ. Sci. Technol.* **2023**, *57*, 15747−15758.
(24) Nishiumi, M.; Miura, H.; Wada, K.; Hosokawa, S.; Inoue, M. Active Ruthenium Catalysts Based on Phosphine-Modified Ru/CeO_2 for the Selective Addition of Carboxylic Acids to Terminal Alkynes. *ACS Catal.* **2012**, *2*, 1753−1759.
(25) Kikugawa, M.; Goto, Y.; Kobayashi, K.; Nanba, T.; Matsumoto, H.; Imagawa, H. Efficient Ammonia Synthesis over Ru/CeO_2-PrO_x Catalysts with Controlled Ru Dispersion by Ru-Pr Interaction. *J. Catal.* **2022**, *413*, 934−942.
(26) Dai, Q. G.; Bai, S. X.; Wang, J. W.; Li, M.; Wang, X. Y.; Lu, G. Z. The Effect of TiO_2 Doping on Catalytic Performances of Ru/CeO_2 Catalysts during Catalytic Combustion of Chlorobenzene. *Appl. Catal., B* **2013**, *142*−*143*, 222−233.
(27) Xu, X. L.; Liu, L.; Tong, Y. Y.; Fang, X. Z.; Xu, J. W.; Jiang, D. E.; Wang, X. Facile Cr^{3+}-Doping Strategy Dramatically Promoting Ru/CeO_2 for Low-Temperature CO_2 Methanation: Unraveling the Roles of Surface Oxygen Vacancies and Hydroxyl Groups. *ACS Catal.* **2021**, *11*, 5762−5775.
(28) Li, C. Y.; Zhang, Z. C.; Zheng, Y. P.; Fang, B. Y.; Ni, J.; Lin, J. X.; Lin, B. Y.; Wang, X. Y.; Jiang, L. L. Titanium Modified Ru/CeO_2 Catalysts for Ammonia Synthesis. *Chem. Eng. Sci.* **2022**, *251*, No. 117434.
(29) Chen, L.; Zhou, W. W.; Huo, C.; Li, L.; Cui, M. F.; Qiao, X.; Fei, Z. Y. Improved Metal-Support Interaction in Ru/CeO_2 Catalyst via Pasma-Treated Strategy for Dichloroethane Oxidation. *Appl. Catal. A-Gen.* **2023**, *660*, No. 119215.
(30) van Raak, T.A.B.J.; Li, S.; Gallucci, F. Prevailing Surface Reactions in the Plasma-Catalytic Ammonia Synthesis with Ru/CeO_2 and Ru/Ti-CeO_2. *Chem. Eng. J.* **2023**, *455*, No. 140691.
(31) Liu, P. F.; Zheng, C. L.; Liu, W.; Wu, X. D.; Liu, S. Oxidative Redispersion-Derived Single-Site Ru/CeO_2 Catalysts with Mobile Ru Complexes Trapped by Surface Hydroxyls Instead of Oxygen Vacancies. *ACS Catal.* **2024**, *14*, 6028−6044.
(32) Yang, C. M.; Lu, Y. X.; Zhang, L.; Kong, Z. J.; Yang, T. Y.; Tao, L.; Zou, Y. Q.; Wang, S. Y. Defect Engineering on CeO_2-Based Catalysts for Heterogeneous Catalytic Applications. *Small Struct.* **2021**, *2*, No. 2100058.
(33) Li, Y. F.; Qin, T.; Wei, Y. C.; Xiong, J.; Zhang, P.; Lai, K. Z.; Chi, H. J.; Liu, X.; Chen, L. W.; Yu, X. L.; Zhao, Z.; Li, L.; Liu, J. A Single Site Ruthenium Catalyst for Robust Soot Oxidation without Platinum or Palladium. *Nat. Commun.* **2023**, *14*, 7149.
(34) Fan, L. L.; Wang, K.; Xu, K. J.; Liang, Z. Y.; Wang, H. P.; Zhou, S. F.; Zhan, G. W. Structural Isomerism of Two Ce-BTC for Fabricating Pt/CeO_2 Nanorods toward Low-Temperature CO Oxidation. *Small* **2020**, *16*, No. e2003597.
(35) Kar, A. K.; Kaur, S. P.; Kumar, T. J. D.; Srivastava, R. Efficient Hydrogenolysis of Aryl Ethers over Ce-MOF Supported Pd NPs under Mild Conditions: Mechanistic Insight Using Density Functional Theoretical Calculations. *Catal. Sci. Technol.* **2020**, *10*, 6892−6901.
(36) Chen, B.; Zeng, X.; Liu, Y.; Xiao, F.; Huang, M.; Bing Tan, K.; Cai, D.; Huang, J.; Zhan, G. Thermal Decomposition Kinetics of M-BTC (M = Cu, Co, Zn, and Ce) and M-BTC/Pt Composites under Oxidative and Reductive Environments. *Chem. Eng. J.* **2022**, *450*, No. 138470.
(37) Sivan, S. E.; Kang, K. H.; Han, S. J.; Francis Ngome Okello, O.; Choi, S.-Y.; Sudheeshkumar, V.; Scott, R. W.J.; Chae, H.-J.; Park, S.; Lee, U-H. Facile MOF-Derived One-Pot Synthetic Approach toward Ru Single Atoms, Nanoclusters, and Nanoparticles Dispersed on CeO_2 Supports for Enhanced Ammonia Synthesis. *J. Catal.* **2022**, *408*, 316−328.
(38) Tan, W.; Wang, J.; Yu, S.; Liu, A.; Li, L.; Guo, K.; Luo, Y.; Xie, S.; Gao, F.; Liu, F.; Dong, L. Morphology-Sensitive Sulfation Effect on Ceria Catalysts for NH_3-SCR. *Top. Catal.* **2020**, *63*, 932−943.
(39) Liu, K.; You, H. P.; Jia, G.; Zheng, Y. H.; Huang, Y. J.; Song, Y. H.; Yang, M.; Zhang, L. H.; Zhang, H. J. Hierarchically Nanostructured Coordination Polymer: Facile and Rapid Fabrication and Tunable Morphologies. *Cryst. Growth Des.* **2010**, *10*, 790−797.
(40) Loridant, S. Raman Spectroscopy as a Powerful Tool to Characterize Ceria-Based Catalysts. *Catal. Today* **2021**, *373*, 98−111.
(41) Tan, W.; Xie, S. H.; Cai, Y. D.; Yu, H. W.; Ye, K. L.; Wang, M. Y.; Diao, W. J.; Ma, L.; Ehrlich, S. N.; Gao, F.; Dong, L.; Liu, F. D. Surface Lattice-Embedded Pt Single-Atom Catalyst on Ceria-Zirconia with Superior Catalytic Performance for Propane Oxidation. *Environ. Sci. Technol.* **2023**, *57*, 12501−12512.
(42) Wang, F.; Li, C. M.; Zhang, X. Y.; Wei, M.; Evans, D. G.; Duan, X. Catalytic Behavior of Supported Ru Nanoparticles on the {1 0 0}, {1 1 0}, and {1 1 1} Facet of CeO_2. *J. Catal.* **2015**, *329*, 177−186.
(43) Sato, K.; Zaitsu, S.; Kitayama, G.; Yagi, S.; Kayada, Y.; Nishida, Y.; Wada, Y.; Nagaoka, K. Operando Spectroscopic Study of the Dynamics of Ru Catalyst during Preferential Oxidation of CO and the Prevention of Ammonia Poisoning by Pt. *JACS Au* **2022**, *2*, 1627−1637.
(44) Liu, Z.; Lu, Y.; Confer, M. P.; Cui, H.; Li, J.; Li, Y.; Wang, Y.; Street, S. C.; Wujcik, E. K.; Wang, R. Thermally Stable RuO_x-CeO_2 Nanofiber Catalysts for Low-Temperature CO Oxidation. *ACS Appl. Nano Mater.* **2020**, *3*, 8403−8413.
(45) Wang, Y. F.; Wang, R. G. Effects of Chemical Etching and Reduction Activation of CeO_2 Nanorods Supported Ruthenium Catalysts on CO Oxidation. *J. Colloid Interface Sci.* **2022**, *613*, 836−846.
(46) Qin, X. X.; Chen, X. Y.; Chen, M.; Zhang, J. H.; He, H.; Zhang, C. B. Highly Efficient Ru/CeO_2 Catalysts for Formaldehyde Oxidation at Low Temperature and the Mechanistic Study. *Catal. Sci. Technol.* **2021**, *11*, 1914−1921.
(47) Vayssilov, G. N.; Lykhach, Y.; Migani, A.; Staudt, T.; Petrova, G. P.; Tsud, N.; Skala, T.; Bruix, A.; Illas, F.; Prince, K. C.; Matolin, V.; Neyman, K. M.; Libuda, J. Support Nanostructure Bboosts Oxygen Transfer to Catalytically Active Platinum Nanoparticles. *Nat. Mater.* **2011**, *10*, 310−315.
(48) Muravev, V.; Spezzati, G.; Su, Y. Q.; Parastaev, A.; Chiang, F. K.; Longo, A.; Escudero, C.; Kosinov, N.; Hensen, E. J. M. Interface Dynamics of Pd-CeO_2 Single-Atom Catalysts during CO Oxidation. *Nat. Catal.* **2021**, *4*, 469−478.
(49) Chen, J.; Xiong, S.; Liu, H.; Shi, J.; Mi, J.; Liu, H.; Gong, Z.; Oliviero, L.; Mauge, F.; Li, J. Reverse Oxygen Spillover Triggered by CO Adsorption on Sn-doped Pt/TiO_2 for Low-Temperature CO Oxidation. *Nat. Commun.* **2023**, *14*, 3477.
(50) Lin, B. Y.; Liu, Y.; Heng, L.; Wang, X. Y.; Ni, J.; Lin, J. X.; Jiang, L. L. Morphology Effect of Ceria on the Catalytic Performances of Ru/CeO_2 Catalysts for Ammonia Synthesis. *Ind. Eng. Chem. Res.* **2018**, *57*, 9127−9135.
(51) Lin, B. Y.; Fang, B. Y.; Wu, Y. Y.; Li, C. Y.; Ni, J.; Wang, X. Y.; Lin, J. X.; Au, C. T.; Jiang, L. L. Enhanced Ammonia Synthesis Activity of Ceria-Supported Ruthenium Catalysts Induced by CO Activation. *ACS Catal.* **2021**, *11*, 1331−1339.
(52) Xie, S. H.; Ye, K. L.; Du, J. S. S.; Zhang, X.; Kim, D. K.; Loukusa, J.; Ma, L.; Ehrlich, S. N.; Marinkovic, N. S.; Yoreo, J. J. D.; Liu, F. D. Ru/MgO Catalyst with Dual Ru Structure Sites for Efficient CO Production from CO_2 Hydrogenation. *Chem. Eng. J.* **2024**, *487*, No. 150486.
(53) Wu, X. D.; Zhang, L.; Weng, D.; Liu, S.; Si, Z. C.; Fan, J. Total Oxidation of Propane on Pt/WO_x/Al_2O_3 Catalysts by Formation of

Metastable $Pt^{\delta+}$ Species Interacted with WO_x Clusters. *J. Hazard. Mater.* **2012**, *225−226*, 146−154.
(54) Fang, Y. R.; Li, L.; Yang, J.; Hoang, S.; Wang, L. M.; Xu, J.; Yang, W. W.; Pan, C. Q.; Zhu, Y. H.; Deng, H. T.; Luo, Z.; Sun, C. Z.; Gao, D. Q.; Li, Z. G.; Guo, Y. B. Engineering the Nucleophilic Active Oxygen Species in $CuTiO_x$ for Efficient Low-Temperature Propene Combustion. *Environ. Sci. Technol.* **2020**, *54*, 15476−15488.
(55) Chen, L. G.; Zhu, Y. L.; Zheng, H. Y.; Zhang, C. H.; Li, Y. W. Aqueous-Phase Hydrodeoxygenation of Propanoic Acid over the Ru/ZrO_2 and Ru-Mo/ZrO_2 Catalysts. *Appl. Catal. A-Gen.* **2012**, *411−412*, 95−104.
(56) Hoost, T. E.; Laframboise, K. A.; Otto, K. Co-Adsorption of Propene and Nitrogen Oxides on Cu-ZSM-5: An FTIR Study. *Appl. Catal., B* **1995**, *7*, 79−93.

https://doi.org/10.1021/acs.est.4c07159
Environ. Sci. Technol. 2024, 58, 19533−19544